3

EXPERIMENTAL TECHNIQUES

This chapter consists of a description of the sample preparation and of the important techniques used for growth and characterization of the Fe/CoO bilayer system. A short introduction in the experimental methods is also provided. They are described in a "chronological" order, from cleaning the substrate to synchrotron radiation–based techniques to study the electronic and magnetic properties of the Fe/CoO bilayers.

Contents

3.1 Sample growth

3.1.1 Substrate preparation

The experiments have been performed under ultrahigh-vacuum (UHV) conditions at a base pressure in the lower 10^{-10} mbar range in chambers[1] equipped with the main tools for sample preparation and surface characterisation. The principle layout of one the chamber (chamber also used for the synchrotron experiments) used for the structural characterization as well as for magneto-optical Kerr effect (MOKE) measurements is depicted in Fig. 3.1. A disk-shaped Ag(001) single crystal of 8 mm in diameter and 2 mm in height provided by Matek GmbH [64] served as a non-magnetic substrate. The single crystal was cut in order to assure a miscut angle of less than $0.2°$.
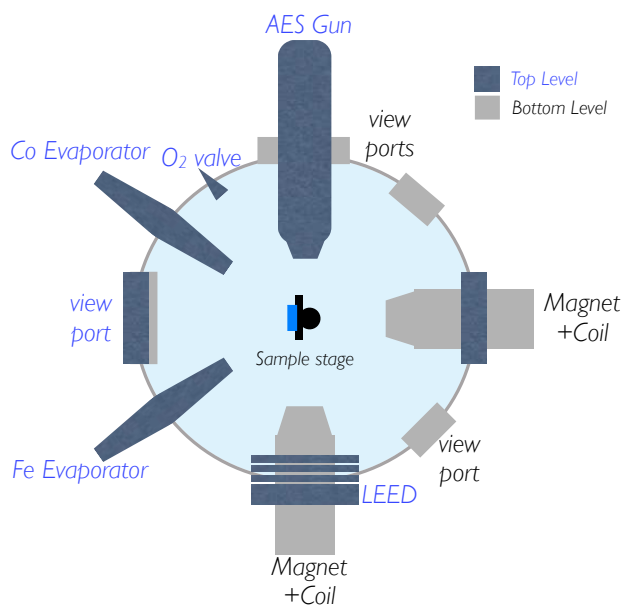

Figure 3.1: Schematic drawing of the preparation chamber used in this work. The top level was used for deposition, AES, and LEED, and the bottom level for MOKE experiments.

A clean Ag(001) surface was prepared by sputtering in an Argon atmosphere at a pressure in the lower 10^{-5} mbar range. The bombardment with 600–650 eV Ar^+ ions led to typical sample currents of about 1.4 μA [2]. Auger electron spectroscopy (AES) was used to check the purity of the substrate before

---

[1]In this work, different UHV chambers were used depending on what kind of experiments were performed.

[2]Note that the sample current value can change for different sputtering geometries, since gun-to-sample distance is playing an important role.

annealing at a temperature of about 650 K for 10 min. Temperatures were measured by two N-type thermocouples closely attached to the sample. The thermal treatment after sputtering was performed in order to reestablish a smooth and defect-free substrate surface. Low energy electron diffraction (LEED) was employed to probe the crystalline long-range order of the sample surface. Multiple sputtering–annealing cycles were performed in order to assure the surface quality.

3.1.2   Layer deposition

Each metal was evaporated from a separate source by means of electron beam assisted heating of high purity material rods (Fe, Co: 99.99%). A detailed description of the evaporator, although a slightly modified version, is described in Ref. [65]. In short, electrons thermally emitted from a heated tungsten filament, are accelerated in a concentric electrostatic field to the tip of the rod, which is held at positive potential ($\approx$1 kV). The heating power, which was typically between 5–20 W, can be adjusted by the filament current, the rod potential and the tip-to-filament distance. An integrated fluxmeter, which senses the ionised atoms in the vapour, provides, if calibrated, a direct measure of the evaporation rate. Stable and reproducible deposition rates can be achieved, if constant evaporator parameters and a constant tip-to-filament geometry can be maintained [66].

CoO was prepared by deposition of the Co on the Ag(001) substrate in an oxygen atmosphere with a pressure of 10^{-6} mbar. The CoO layer was prepared only as continuous film. The Fe layer was always deposited on top, after a previous annealing of the oxide layer. The layer thickness was determined after a previous calibration of the evaporators by looking at the medium energy electron diffraction (MEED) oscillations of Fe and Co on a Cu(001) substrate [66]. An AES calibration table was used to cross-check the thickness calibration. For the experiments at the beamline, the edge-jump of X-ray absorption spectra was employed to check the thickness reproducibility. The estimated error in thickness determination for both layers is less than 10%.

For spectroscopy experiments, both layers were prepared as single continuous films of different thicknesses. After each layer deposition, AES and LEED were employed to check the sample's chemical and structural composi-
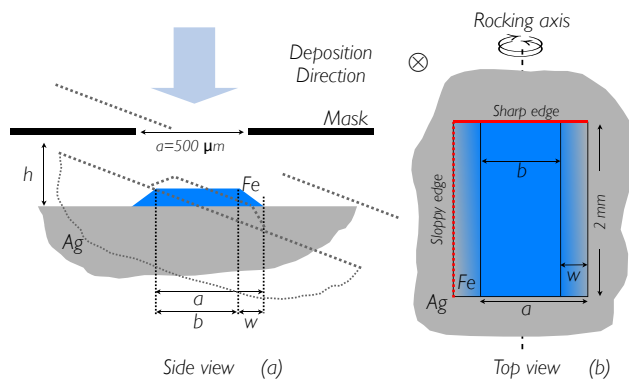
Figure 3.2: Principle of wedge preparation: A mask made of a thin copper foil with a rectangular aperture of 2.0 mm × 0.5 mm is placed at a distance h closely in front of the sample (8 mm in diameter). Rocking the unit of sample and mask about the axis parallel to the long side of the aperture during film deposition yields a plateau of width b and two wedges of width w on both sides of the plateau. The aperture width a is reproduced in the wedge structure as the sum of b and w.

tion.

For the PEEM experiments, Fe films were grown in the form of wedges by a mask technique. The principle is illustrated in Fig. 3.2. A mask with a rectangular aperture of 2.0 mm × 0.5 mm was closely placed in front of the sample. During the deposition, the unit of mask and sample was slowly rocked by a stepping motor-driven manipulator at a speed of 2°/s about the axis that is parallel to the long side of the aperture. This deposition arrangement yields a film structure with a plateau and a wedge on both sides of the plateau. The actual aperture width of $a = 500$ μm is reproduced on the sample as the sum of plateau width b and wedge width w. These widths can easily be identified from PEEM images taken in the survey mode and therefore provide a readily accessible scale. The width of the wedge is defined by the amplitude of the rocking angle θ, and the distance h between aperture and sample as $w = 2h \tan \theta$. This relation allows a convenient estimation of h since w can be extracted from PEEM images too, while this is not possible for h.

3.2 Sample characterization techniques

3.2.1 Auger electron spectroscopy

Auger electron spectroscopy (AES) was developed as a technique in the late 1960's, its name deriving from the first one observing the effect – the french physicist Pierre Auger. It can be used as a surface sensitive technique using the emission of low energy electrons (energies in the range 50–1500 eV and electron mean free paths in the 5–50 Å range). It is a very common surface analytical technique for determining the composition of surfaces.
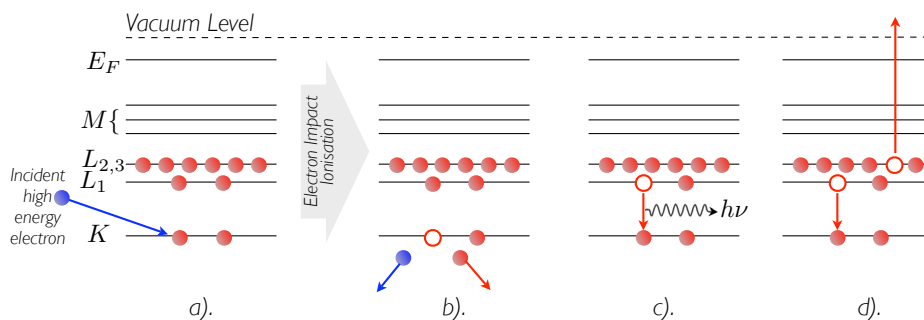

Figure 3.3: Schematic representation of the Auger process exploited in AES. Ionization of the atom (a, b) and the creation of a core-hole. Radiative relaxation by emission of a photon (c) or non-radiative: an Auger electron is emitted (d).

Auger spectroscopy involves three basic steps:

- **Ionisation**: The Auger process is initiated by the creation of a core hole - this is typically carried out by exposing the sample to X rays (energy 1–2 keV) or a beam of high energy electrons (primary energy in the range 2–5 keV) as shown in Fig. 3.3 (a, b). Such particles have sufficient energy to ionise all levels of the lighter elements, and higher core levels of the heavier elements. In the figure, ionisation is shown to occur by removal of a K-shell electron, but in practice, ions with holes in a variety of inner shell levels are common.

- **Relaxation and Auger Emission**: The ionised atom that remains after the removal of the core hole electron is in a highly excited state and will rapidly decay to a lower energy state either by: X-ray fluorescence [Fig. 3.3 (c)], or Auger emission (d).
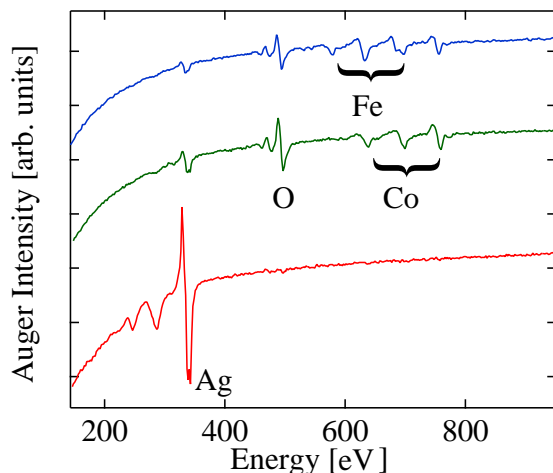
Figure 3.4: AES spectra for the clean Ag surface (bottom), 5 ML CoO/Ag (middle), and 1.5 ML Fe/5 ML CoO/Ag (top).

- **Analysis of the emitted Auger electrons**: Auger electrons are not the only electrons emitted from a solid when probed by 3 keV electrons. Most of the emitted electrons are inelastically scattered electrons. A plot of the number of electrons emitted from the solid with a given kinetic energy, N(E), would display only a small peak at any particular Auger electron transition energy. In order to enhance the detection of Auger electron peaks, the spectrum of N(E) is differentiated by using a lock-in technique. The energy of the emitted electrons is analysed using, for example, a Retarding Field Analyzer (RFA) with a grid-variable potential.

In summary, Auger Electron Spectroscopy (AES) is a surface-sensitive spectroscopic technique used for elemental analysis of surfaces and it offers:

- high sensitivity (typically 1% of an atomic monolayer for all elements, except H and He);

- a measure of surface cleanliness of samples;

- quantitative compositional analysis of the surface region of specimens (by comparison with standard samples of known composition).

In this work a Staib Instruments CMA-type double pass analyzer [67] with a working distance of 12 mm was used. The e-beam energy of the electron gun was set to 3 keV. The lower AES spectrum (Fig. 3.4) shows the characteristic Auger spectrum of Ag – the absence of other features proves the chemical cleanness of the surface. After depositing 5 ML CoO on this surface, the spectrum changes drastically, four different peaks appearing: the one at 510 eV represents

the oxygen, and the three peaks at 656 eV, 715 eV, and 775 eV mark the appearance of Co on the surface. As a next step 1.5 ML Fe have been added on top of this 5 ML CoO, and the appearance of another three peaks occurs at 598 eV, 651 eV and 703 eV. The gain in intensity of the first two Co peaks is due to the superposition of Fe and Co intensities at nearly the same energies. One should note here also the behavior of the Ag peak at 353 eV which is loosing its intensity due to the damping of the electrons in the solid (finite probing depth effect).

### 3.2.2   Low energy electron diffraction

Low energy electron diffraction (LEED) is a well known surface science technique [68, 69, 70] proposed for the first time in 1927 by Davidson and Germer [71]. For more than 50 years LEED has been the main technique used to study the morphology and structure of two-dimensional planar surfaces.

Normal incidence low-energy electrons (30–500 eV) give access to the structure of the surface. The wavelengths are comparable to the spacing between atoms both parallel and perpendicular to the crystal surface, hence, for an ordered surface, the electrons might diffract through elastic back-scattering. Since the cross section for scattering of low-energy electrons is very large, an incident electron beam is damped within a few surface layers. The backscattering is strongly dependent on the type of atoms and may be used in one of two ways:

- **Qualitatively**: The diffraction pattern is recorded, and only the spot positions are used to extract the size, symmetry, and rotational alignment of the adsorbate unit cell with respect to the substrate unit cell. A surface layer on a crystal can be described as a two-dimensional grid of atoms. From this grid, the reciprocal lattice can be constructed with help of the LEED patterns.

- **Quantitatively**: The intensities of the various diffracted beams are recorded as a function of the incident electron beam energy to generate so-called *I(E)* curves which, by comparison with theoretical curves for example, may provide accurate information on atomic positions. This approach needs the use of the complex theory of multiple scattering. Theoretical models for LEED spectra can be found in [68, 69, 70, 72]

Experimentally, a well-collimated monoenergetic beam of electrons, created by

Figure 3.5: LEED picture of a clean Ag(001) surface (a) and energy dependent (00) spot intensity [*I(E)* spectra] for clean Ag (b). Small and intense spots prove high crystallinity of the sample. The reciprocal unit cell, recording energy and crystallographic orientations are indicated.
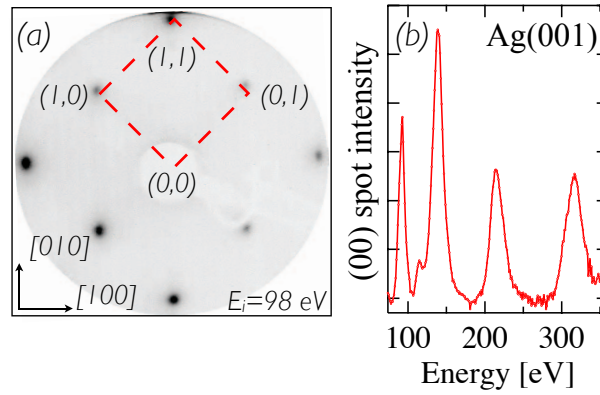
an electron gun, impinges on a clean sample surface, usually at normal incidence. The diffracted electrons "radiate out" from the sample toward a display detector, passing through a retarding field.

Medium energy electrons can also be used to investigate the structure of surfaces. In order to extract structural information from the diffraction of medium energy electrons, the technique has to be adapted. The easiest way of doing this is to use a reflection geometry in which the electron beam is incident at a very grazing angle – it is then known as Medium Energy Electron Diffraction (MEED).

A simple theory of peak formation for LEED *I(E)* depicted by Pendry [73] in the 1970'es suggested that although the electrons do not penetrate deeply into the crystal, one can suppose, especially at relatively high energies, that they do go sufficiently deep into the sample to be sensitive enough to the periodic lattice of the crystal on the perpendicular (*z*) direction. The energy sweep in this LEED *I(E)* experiments is the equivalent to a variation of the momentum transfer vector along the surface truncation rods in reciprocal space. Even though there are better techniques doing that (all based on X-ray diffraction), a kinematic evaluation of LEED *I(E)* curves of the specular (00) spot enables one to calculate the vertical interatomic layer spacing with a reasonable accuracy. In the kinematic approximation the layer spacing is derived from the position of a set of Bragg peaks. The interlayer spacing d is given by:

$$d = \frac{nh}{2\cos\theta\sqrt{2m_e(E(n) - U_0)}} \tag{3.1}$$

where θ, m_e and h denote the angle between sample normal and incident electron beam, electron mass, and Planck's constant, respectively. $E(n)$ is the energy

of the electrons outside the crystal corresponding to a Bragg peak of the order n. U_0 is the correction added because the wavelength of the electrons changes after they enter the crystal from vacuum due to the "inner potential" well of the crystal. U_0 represents the real part of the complex inner potential, the energy difference between the vacuum level and the plateau of the muffin-tin potential. The value of the vertical lattice spacing d can be retrieved from a linear regression of $E(n)$ versus n^2. The slope of this line yields the value of d, and the intersect with the E axis gives U_0.

It has to be stipulated here that d has to be interpreted as an averaged interlayer distance of the first few monolayers. More precise methods involve sophisticated dynamical theories (*i.e.* Barbier-van Hove Tensor LEED calculation package). The method presented here was successfully applied for $3d$ metals and alloys [66, 74].

In this work was mainly used an Omicron LEED system [75] with a three-grid retarding field analyzer. Figure 3.5 (a) provides an example of a diffraction pattern of a clean single crystalline Ag(001) surface. The specular (00) spot is obscured by the electron gun. The diffraction pattern reflects the fourfold symmetry of the sample. The diffraction spots are labeled by their corresponding Miller indices (*hk*) of a two-dimensional lattice according to the common notations. The sharp and intense spots are a good indication for a clean, smooth surface with a high structural ordering.

Positions of diffracted beams in the elastic diffraction pattern give the surface unit cell of the crystal, but no information about disposition of contents of the cell, such as separation between the crystallographic planes of atoms near the surface sample or the relative location of the adsorbates to the substrate. This information can be found in the *I(E)* curves of the elastically scattered beams measured as a function of energy or incidence angle. We reproduce in Fig. 3.5 (b) the intensity of the specularly reflected (00) beam as a function of energy from a Ag(001) surface under the condition of near-normal incidence. The crystal has been rotated about one axis by $\alpha = 5°$ in order to allow the (00) spot to get unframed by the electron gun. More detailed information about LEED-*I(E)* technique, concerning data analysis, will be presented in Chapter 4.

3.2.3   Scanning tunneling microscopy

Since the success of the first experiments by G. Binning, H. Rohrer [76, 77] and coworkers from IBM Zürich in 1981, Scanning tunneling microscopy (STM) has developed into one of the most successful techniques in surface science analysis.

In STM, an atomically sharp metal tip is brought within a few angstroms distance to the conducting surface to be studied as shown in Fig. 3.6. The tip-sample distance s (< 10 Å) is the tunneling barrier. A bias voltage (V_T) is applied to the system, and a tunneling current (I_T) is measured between the tip and the sample as $I_T \propto V_T e^{-s}$.

There are two different modes of operation for a scanning tunneling microscope:

- In **constant height mode**, the tip is not moved up or down as it scans the surface. The change in the tip to surface distance by the topography of the sample gives a resulting change in the measured current. This mode allows for faster scanning and is usually used on smooth or atomic scale images;

- In **constant current mode**, the tip moves up and down as it scans the surface. This vertical motion is used to maintain a constant measured tunneling current. This mode is usually used on rough or large scale images so that the tip does not crash into the surface.

It should now be clear that STM images are really contour maps that indicate the change in measured tunneling current (constant height mode) or the change in the vertical tip position (constant current mode) as the tip scans the surface. By convention, regions of high current are depicted by bright regions in the STM image. Regions of low tunneling current appear darker in the image.

To a rough approximation, this variation in current is directly related to the topography of the surface. This is especially true for metallic surfaces. Unfortunately, semiconductors often exhibit a convolution of topographic and electronic factors which make image interpretation difficult. For the oxides, due to their insulating nature, the experiments are hard to follow. But nevertheless, experiments on thin oxide films of CoO, NiO, MnO [60, 44] and TiO_2 [78] have been successfully carried out.

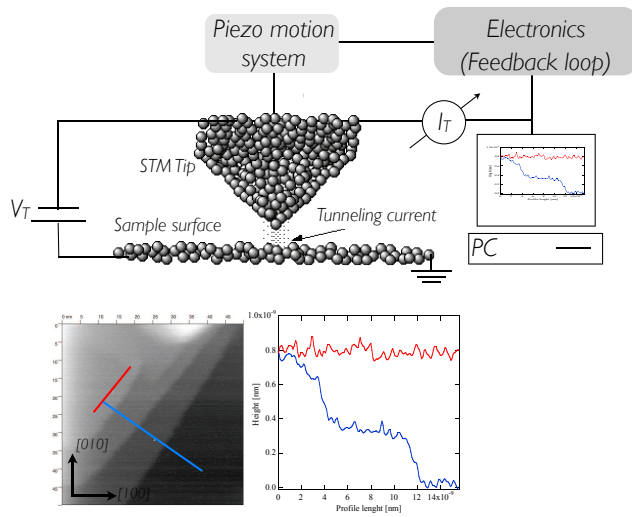The STM used in this work is a UHV STM 1 from Omicron. The micro-

Figure 3.6: Schematic view of the STM principle. The STM is slowly approaching the sample (manually or/and automatically). A voltage is applied between the sample and the tip (V_T) and the tunneling current is read (I_T). The tip is scanning the surface driven by a piezo-electric system. The image shows a clean Ag surface, source of the contrast being the topography of the surface. The graph represent line scans on the terrase (red) and perpendicular to the surface step edges (blue).

scope was mounted onto an existing vacuum system. The concept allows easy access to the microscope and to the sample/tip storage carousel and avoids interferences to other techniques. An easy-to-use, pincer-grip wobble stick is used for fast transfer action between the main system manipulator, the sample/tip storage carousel and the sample acceptor in the STM. An internal spring suspension system with eddy-current damping improves the vibration isolation. An in-vacuum I/V converter close to the tip provides lowest noise conditions. The tips were prepared form W wire by electro-chemical etch in NaOH following the procedure described in Ref. [79].

3.2.4   Magneto optical Kerr effect

The magneto-optical Kerr effect (MOKE) was used here for measuring magnetic hysteresis loops. The effect was discovered by J. Kerr in 1877, and was adapted to study surface magnetism in 1985 by Moog and Bader [80, 81]. The magneto-optical Kerr effect relies on the response of optical properties on the magnetic state of a sample. The magneto-optical interaction causes a polarization change upon reflection of polarized light from a magnetic surface. The reflection of linearly polarized light impinging on the sample leads to a rotation of the polarization axis and to the appearance of a small fraction of elliptically polarized
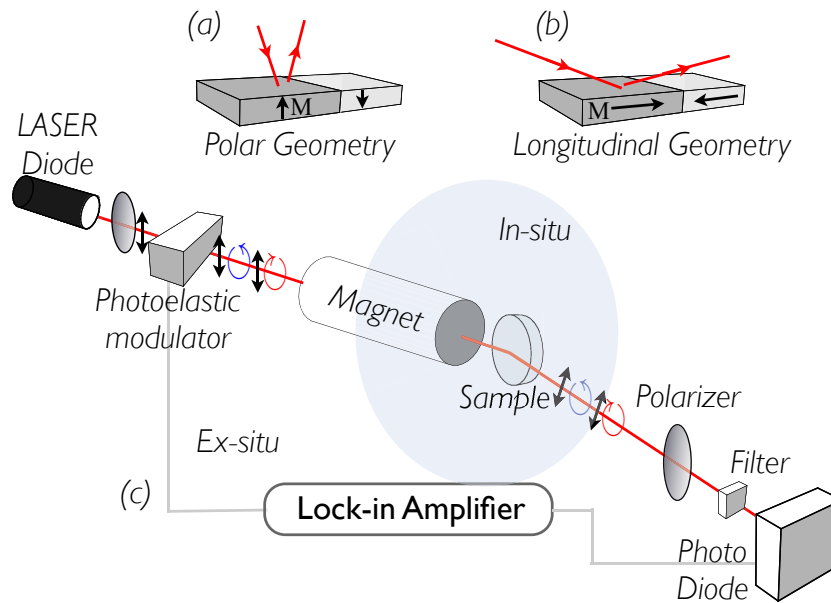
Figure 3.7: Polar (a) and longitudinal (b) geometry for MOKE. The polar MOKE geometry (a) gives the highest signal at normal incidence and is sensitive to the out-of-plane component of the magnetization. In the longitudinal geometry (b) the linearly polarized light beam is inclined with respect to the surface and probes the in-plane component of the magnetization (c). The MOKE system, set up in this work, employs a photoelastic modulator which modulates the polarization state of linearly polarized light with an amplitude $\lambda/4$ at a frequency f. The polarization axis makes an angle of $45°$ relative to the modulation axis. The $2f$ signal from the photodiode is proportional to the Kerr rotation.

light in the reflected beam. The former effect is quantified by the so-called Kerr angle and the latter by the Kerr ellipticity. Both quantities are proportional to the magnetization within the probing volume, but do also depend on wavelength and studied material. The probing depth is given by the penetration depth of the light, which is of the order of a few hundred Å.

There exist different MOKE geometries, depending on the orientation of the magnetization vector **M** relative to the incidence plane. In the polar geometry, as illustrated in Fig. 3.7 (a), the polarized light beam hits the surface close to normal incidence. This geometry is sensitive to an out-of-plane magnetization. In the longitudinal geometry [Fig. 3.7 (b)], the magnetization lies within the surface plane and also within the plane of incidence. And in the transverse geometry (not shown), the magnetization lies within the surface plane but or-

thogonal to the plane of incidence.

The MOKE system used in the present experiments is a setup based on a polarization-modulation technique. A scheme is sketched in Fig. 3.7 (c). An intensity-stabilised 5 mW laser diode emitting partially polarized light at a wavelength of $\nu = 670$ nm acts as a light source. The key element of this set-up is a photoelastic modulator which consists of a transparent piezo-driven bire-fringent crystal. The modulation axis is set at $45°$ relative to the polariser. The electric field component of the light pointing along the modulation axis receives a periodic retardation at the modulation frequency $f = 50$ kHz with an ampli-tude of $\lambda/4$. Thus, the polarization state of the modulated light is changed pe-riodically according to the following sequence: linear, right-circular, linear and left-circular, whereas it is elliptically polarized in between. The linear compo-nent experiences a Kerr rotation upon reflection by the sample. Eventually, the reflected light passes an analyser and a 670 nm interference filter before being detected by a photodiode. The preamplified output signal from the photodiode as well as a reference signal from the modulator are fed into a lock-in amplifier. It can be shown that the Kerr rotation yields an AC signal at twice the modula-tion frequency [82]. This $2f$ signal is recorded and normalised to the DC signal, while a computer controlled bipolar power supply sweeps the current of the magnet coil. The *in-situ* coil provides a maximum field of about 20 kA/m at the sample position. Longitudinal geometry was achieved by a set-up where the light from a second laser diode has to pass a pinhole in the coil. In this case the sample normal is oriented perpendicular to the magnetic field. The same analyser and photodiode are used for both MOKE geometries.

3.2.5   Polarized soft X-ray spectro-microscopy

Source of polarized X rays

All the measurements presented in this work were performed at the beam-line UE56/2-PGM2 of the BESSY synchrotron radiation source in Berlin. The insertion device is an elliptical double undulator with an undulation period of 56 mm. The monochromator used was a PGM-type one (Planar Grating Monochromator). UE56/2 was designed to emit light in the energy region of 100–1300 eV with tunable polarization and an energy resolution of about 100 meV at the 650–850 eV energy range. The elliptical double undulator provides

both helicities of circularly polarized light as well as linearly polarized light with a polarization axis horizontal or vertical with respect to the storage ring plane. The degree of circular polarization, which is set by the relative horizontal shift of the undulator elements, is about 85% in the energy region 650–850 eV. The beamline is thus providing all the "light" demands for metals and oxides spectro-microscopy experiments [83].

X-ray absorption spectroscopy

In the X-ray absorption process, a core electron is excited to an empty state and, as such, X-ray absorption spectroscopy probes the unoccupied part of the electronic structure of the system. An important aspect of the usefulness of XAS is that one is able to obtain element-specific information. This implies that if two or more inequivalent types of the same atoms are present, the spectral shape is a linear combination of all the individual sites [84].

There are different methods of detection used in X-ray absorption spectroscopy:

- **Transmission:** In this case, the intensity of the X rays is measured before and after passing through the sample, and the percentage of transmitted X rays is determined. The final XAS spectrum is just a repetition of this experiment for the whole range of energies. Transmission mode experiments are standard for hard X rays. For soft X rays, the substrate has to be thin (less then 0.1 μm) in order to get a detectable signal. Because of the large cross section of the soft X rays with air, all the experiments have to be performed in vacuum.

- **Fluorescence yield detection:** In this case, the detector is a photodiode detecting the X-ray fluorescence signal from the sample in the X-ray beam. This technique works for insulating samples (which is the case for CoO and NiO single crystalline substrates), but the results are qualitative [85, 86] and can lead to errors that are much larger than the signal. The fluorescence yield method is insensitive to the applied magnetic field, but the yield is intrinsically not proportional to the absorption cross section. It is well adapted for qualitative measurements.

- **Total electron yield detection:** In this case, the measured signal is the drain current appearing in the sample during X-ray irradiation. This drain

current is recorded for each X-ray energy point. However, to get reliable data, a conducting sample (metallic) is needed. The total electron yield method is sensitive to the varying applied magnetic field, with possible effects in changing the electron detecting efficiency, or, equivalently, the sample photo-current. Saturation effects may also appear for thicker films [87]. However, due to the possibility of extracting quantitative data, it is the preferred method in most experiments in the soft X-ray regime and was also used in this work.

Magnetic circular dichroism

In 1975, Erskine and Stern [88] considered excitations between a core state and a valence state and performed a simple calculation on the expected effect for the $M_{3,2}$ edges in metallic Ni. This paper constitutes the birth of what is known as X-ray magnetic circular dichroism (XMCD).

For a system in an external magnetic field, the absorption coefficient μ is related to the imaginary part of the refractive index $\text{Im}(n)$, where n is connected to the dielectric tensor, which is polarization dependent. The dependence of μ on the state of (circular) polarization of the light is called X-ray magnetic (circular) dichroism:

$$XMCD = \frac{\mu^+ - \mu^-}{\mu^+ + \mu^-} \tag{3.2}$$

where (+) and (–) indicate the parallel, respectively antiparallel orientation of the helicity to the majority, respectively minority spins.

The underlying principle is illustrated in Fig. 3.8 (a) for the case of $3d$ metals. The dipole selection rules together with the Clebsch-Gordon coefficients, which govern the absorption process, explain the spin polarized transitions from $2p_{3/2,1/2}$ levels into the empty $3d$ states. In the case of the $2p_{3/2} \rightarrow 3d$ transition the spin polarization of the excited electrons for the absorption of right circularly polarized light is +1/4. The spin polarization changes its sign for opposite helicity. Neglecting spectral broadening caused by the finite energy width of the light, the absorption spectrum can mathematically be described by a convolution of the density of occupied $2p$ states with the density of unoccupied states above the Fermi edge. Due to the exchange-split $3d$ bands, the density of unoccupied states differs for spin-up and spin-down electrons. Thus,
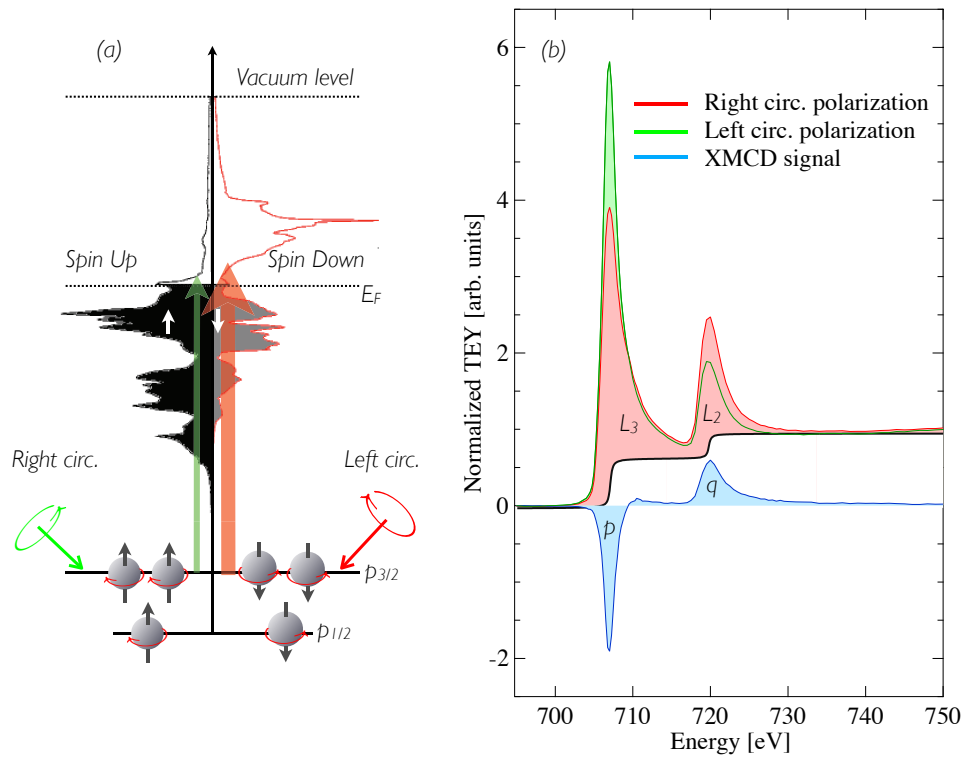
Figure 3.8: Origin of X-ray magnetic circular dichroism in photoabsorption (a): Spin–orbit coupling lifts the degeneracy of the $2p_{3/2,1/2}$ core levels. The absorption of circularly polarized light leads to a spin polarization of the photo-excited electrons. The imbalance of spin-up and spin-down carriers in ferromagnetic $3d$ transition metals gives rise to polarization dependent absorption cross sections. (b) Total electron yield absorption spectra and corresponding XMCD difference spectrum in the region of the Fe $L_{3,2}$ absorption edges from a 6 ML Fe/6 ML CoO/Ag(001) sample. The continuous Fe film was magnetically saturated along the [110] crystallographic direction before the deposition of CoO. magnetization and helicity vector make an angle of approximately 70°. The strong dichroism at the L_3 edge is utilised for XMCD-PEEM experimants.

the transition probability will be enhanced (reduced) in the case where the spin polarized photoelectrons encounter a high (low) density of unoccupied states of carriers with the same spin polarization. In other words, the absorption cross section will be different for left and right circularly polarized light. Owing to the symmetry of the effect, a helicity reversal is equivalent to a rotation of the magnetization by 180°. The different signs and magnitudes of the spin polarizations for $2p_{3/2} \rightarrow 3d$ and $2p_{1/2} \rightarrow 3d$ transitions lead to an opposite dichroism at the corresponding L_3 and L_2 absorption edges. In a second step the $2p$ core hole decays via an Auger or fluorescence process. A cascade of secondary elec-

trons is triggered by the emitted Auger electron. Because of the inelastic nature of the scattering processes involved, the secondary electrons do not carry any information related to magnetic dichroism, but their intensity represents the dichroism of the initial absorption step.

XMCD experiments can be performed, with the same result, in two ways: either the magnetization of the sample is reversed (applying an external magnetic field) while the helicity of the X-ray beam is maintained constant, or the helicity of the beam is reversed at constant magnetization. Then, the difference spectra should present dichroic signals only near the absorption edges like in Fig. 3.8.

Two important sum rules have been derived for XMCD, allowing to deduce element specific orbital and spin magnetic moments from X-ray absorption spectroscopy and its associated magnetic circular dichroism data [89, 90]. Integrating the XMCD curve one can extract two valuable quantities used in the XMCD sum rules: p and q [91]. In a very simple description, since the $L_{2,3}$ splitting appears due to the spin–orbit coupling, linear combinations of p and q values describe in fact the spin and orbital contribution to the magnetic momentum, respectively.

Magnetic linear dichroism

Since its discovery by Gerrit van der Laan in 1986 [17], X-ray magnetic linear dichroism (XMLD) is gaining more and more interest in the field of magnetic thin films or deposited molecules on surfaces.

The electric field vector **E** of linearly polarized soft X rays acts as a search light for the number of empty valence states in different directions of the atomic volume. The anisotropy of the charge in the atomic volume is mainly caused by the anisotropy in the bonding, *i.e.*, the electrostatic potential.

In the absence of magnetic order, the linear dichroism is only a measure of the local charge distribution in the system.

The presence of spin order induces, due to the spin–orbit coupling, a preferred alignment of the local charges relative to the spin orientation of the system. This effect is the basis for the determination of the spin axis in antiferromagnetic and also in ferromagnetic systems by means of XMLD spectroscopy. Since the electric field vector oscillates in time along an axis and the radiation
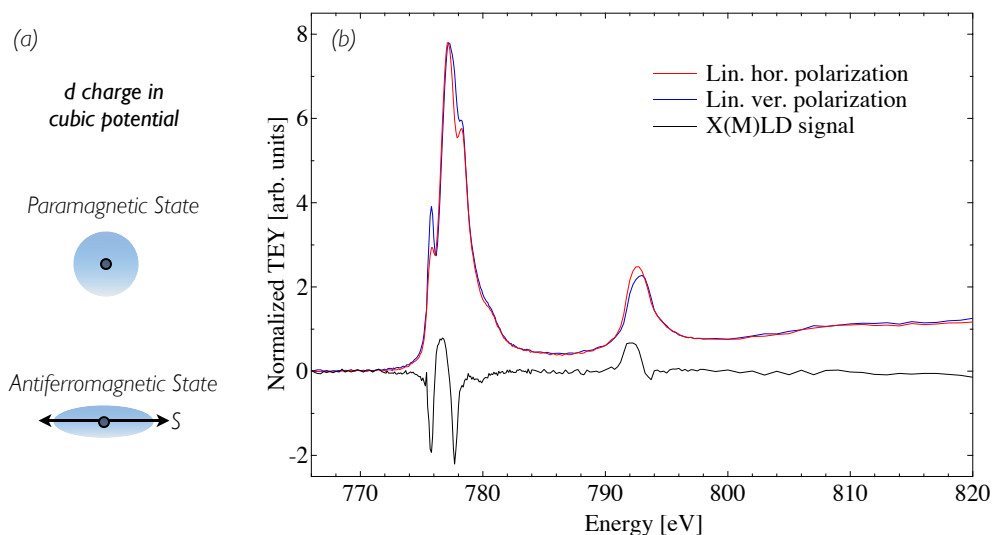
Figure 3.9: Origin of the XMLD effect (a): Due to the cubic symmetry of the CoO lattice, the charge distribution around the atoms is octahedral, thus no linear dichroism is visible in paramagnetic phase (above T_N). Below the Néel temperature, when CoO is antiferromagnetic, the Co spins in the lattice break the cubic symmetry of the charge distribution by spin–orbit coupling. As a consequence the charges in the lattice exhibit a small anisotropy in the unit cell – the charges are now distorted into an ellipsoidal shape in the direction of the spin axis. This charge anisotropy is the reason for the XMLD signal (b) due to the searchlight effect. The spectra are from 6 ML Fe/ 8ML CoO/Ag(001), and the measurement temperature was 150 K.

may be absorbed at any time, linearly polarized X rays are only sensitive to axial, *not* directional properties. Hence, one can determine the orientation of the antiferromagnetic or ferromagnetic axis, but the spin direction itself cannot be determined. It should be mentioned here that an XLD[3] effect can also occur from a structural lifting of the cubic symmetry, as can be seen in Chapter 4.

The maximum XMLD signal is the difference between two spectra obtained with **E** parallel and perpendicular to the magnetic axis. In contrast to the XMCD effect wich varies as $\cos\phi$, the XMLD has a $\cos^2\phi$ angular dependence where ϕ is the angle between the electric field vector **E** and the spin axis.

The X(M)LD signal presented in this work was measured making the difference between the corresponding XAS spectra for horizontal (**E** in the ring plane) linearly and vertically polarized light (**E** perpendicular to the ring plane).

---

[3]Note here the absence of "M" (magnetic) from the abbreviation, emphasizing that the linear dicroism has not necessarily a magnetic origin.

X-ray photoelectron emission microscopy

The idea of cathode lens microscopy was developed beginning at the last century. The increased interest in synchrotron radiation and the success of electron yield absorption spectroscopy lead to the development of the first synchrotron compatible Photoelectron Emission Microscope (PEEM) by Tonner and Harp [92] and few years later by Engel [93]. A more recent review about cathode lens microscopy techniques has been presented by E. Bauer [94]. The magnetic dichroic effects described above are exploited in PEEM as a contrast mechanism for magnetic domain imaging [13, 95]. The power of this technique consist in a combination of the element-specific XMCD [96] and XMLD [95] effects with the features of an electron microscope, *i.e.* sub-micrometer spatial resolution. Thus, PEEM is a suitable technique to study complex magnetic structures composed of chemically different materials. Modern reviews can be found in the references [97, 98, 99].

The photoemission microscope used in this work is a commercially available Focus IS–PEEM [100, 101], with a resolution in threshold photoemission better than 30 nm. The sample is illuminated by UV light or an X-ray beam and located in front of the electrostatic immersion objective lens as shown in Fig. 3.10. The principle of image formation involves an electrostatic tetrode lens and a contrast aperture. During the operation of the microscope, the sample is held at ground potential and the photoemitted electrons are accelerated in an external electrostatic field applied in between the objective lens and the sample of about 5–7 kV/mm. Image contrast can be optimized by a set of circular apertures with different sizes mounted onto a slide which can be positioned *in-situ* by a piezo-driver. This contrast aperture can be conveniently adjusted during the operation of the instrument and its size can be selected between 500 and 30 μm. Non-spherical aberrations are corrected by an electrostatic octupole stigmator inserted into the back focal plane of the objective. In addition, the stigmator may serve as an x, y–deflector. This way the field of view can be changed without moving the sample. The image is magnified by two projective lenses, intensified by a multichannel plate and converted into visible light by means of a scintillator crystal.

The image is then computer recorded with 12-bit resolution by a Peltier–cooled camera (PCO SensiCam). The camera accommodates variable exposure times, with typical image acquisition times of a few seconds to several tens of
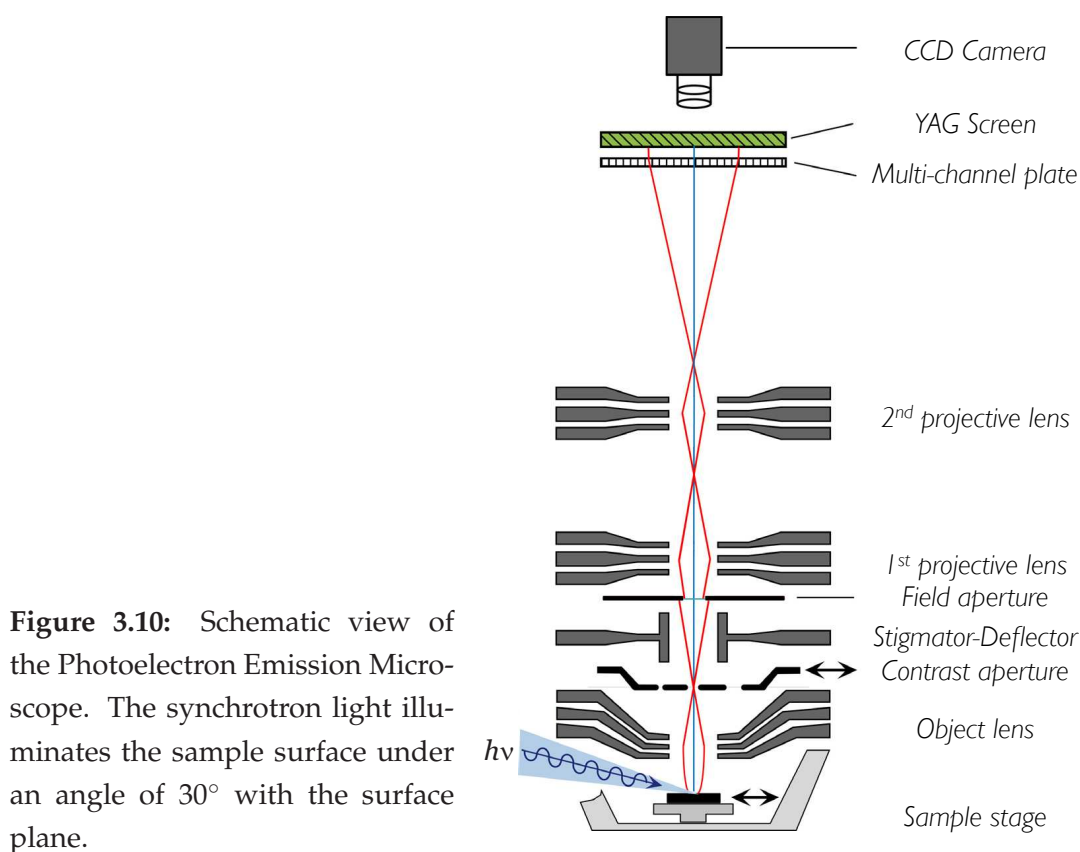
CCD Camera

YAG Screen

Multi-channel plate

2nd projective lens

1st projective lens
Field aperture

Stigmator-Deflector
Contrast aperture

Object lens

hv

Sample stage

Figure 3.10: Schematic view of the Photoelectron Emission Microscope. The synchrotron light illuminates the sample surface under an angle of 30° with the surface plane.

seconds.

The sample forms an integral part of the electron optical column. The sample holder is fixed by three springs in the object plane of the microscope. In this way the uncontrolled motions of the sample relative to the objective lens are greatly reduced, and the image quality is less affected by vibrations. Rotation of the sample is also possible using to a rotational sample stage. The lateral movement of the sample in the object plane is controlled by two orthogonal piezo-driven microslides. These allow a convenient positioning of the sample within a scan area of 4 mm x 4 mm. Within the frame of this work, a liquid N_2 cooling system was adapted to the sample stage allowing also all the degrees of freedom for the translation and rotation of the sample. This provides cooling of the PEEM sample stage, making possible also measurement at temperatures lower than room temperature, allowing measurements carried out at $T < T_N$ of the CoO.

In the PEEM instrument the X rays hit the sample at an angle of 30° relative to the sample surface. This geometry gives an XMCD sensitivity to

both the in-pane and the out-of-plane components of the magnetization vector.

The microscope can be operated in two imaging modes: a survey mode and a high-resolution mode. The high-resolution mode employs high extraction voltages resulting in a field of view down to 20 μm. The survey mode works with low-extraction fields, and the field of view may be as high as 700 μm.

There are different types of contrast mechanisms available in Photoelectron Emission Microscopy:

- **The topological contrast** is due to the distortion of the electric field around different features on the surface [102]. The field distribution distortions disturb the electron trajectory leading to an image contrast.

- **Work function contrast** represents the intensity modulation of the photoemission intensity due to the different emission probabilities in regions with different work functions. Both contrast mechanisms are available also for the UV-PEEM [4].

- **Elemental contrast** is achieved only by tuning the X-ray energies through the absorption edges of the elements. Different areas of the sample containing one chemical element will emit more photoelectrons, thus will appear brighter in the final image.

- **Magnetic contrast** is achieved by making use of the XMCD [13] or XMLD [95] effect. This is the principal contrast mechanism used in this work and will be explained in detail.

The polarization of the incoming synchrotron light can give different contrast in PEEM, taking into account also the magnetization of the studied area. The non-magnetic signal can be removed from the images by changing the helicity of the photons, *i.e.*, in XMCD-PEEM by switching the polarization between left-circular (σ^-) and right-circular (σ^+) polarization. Reversing the helicity reverses only the magnetic contrast but not the non-magnetic one. Thus, the difference image ($\sigma^+ - \sigma^-$) is solely due to the magnetic contrast, whereas the sum of both images ($\sigma^+ + \sigma^-$) contains the non-magnetic contributions only. The actual XMCD-PEEM image in this work is presented as the grayscale–coded normalised asymmetry image defined by ($\sigma^+ - \sigma^-$)/($\sigma^+ + \sigma^-$). Figure 3.11 illustrates this by an example. The images were obtained from an

---

[4]The sample is here illuminated with a UV light source, typically a Hg lamp with $\hbar\omega = 4.9$ eV.

Figure 3.11: Principle of XMCD-PEEM image acquisition: The sample consists of a Fe/CoO bilayer grown on Ag(001). For each helicity an absorption image is recorded with the photon energy tuned to the Fe L_3 absorption edge (707 eV). From these images a background image, which is taken at a pre-edge energy of 695 eV, is subtracted. The background-corrected images for positive (σ^+) and negative (σ^-) helicity show an opposite magnetic contrast. The contrast in the asymmetry image (bottom) has only magnetic origin. The distinct grey scales correspond to mutual perpendicular magnetization directions, as indicated by arrows.
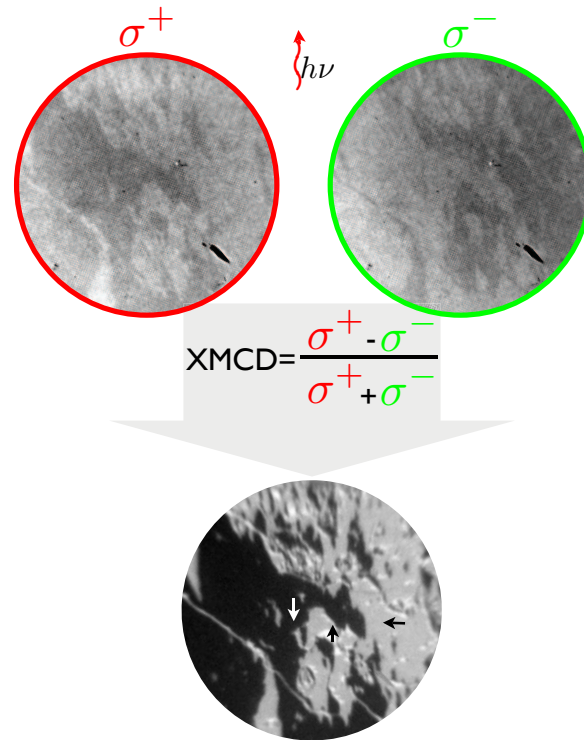
Fe/CoO/Ag(001) sample. The Fe magnetization vector is aligned in the surface plane of the sample. In this case, the images are recorded tuning the photon energy to the Fe L_3 (707 eV) edge. Background correction images (not shown here) are collected at the pre-edge energy of 695 eV. Arrows showing the magnetization direction in each magnetic domain can be depicted analyzing the asymmetry image and taking into account the X-ray direction shown in the figure. Maximum contrast appears between domains with antiparallel magnetization and large projection on the photon direction, since the magnetic contrast varies with the cosine of the angle between the local magnetization and the photon direction. The grey domains have the magnetization vector perpendicular to the dark and bright ones. To get the right orientation of the grey domains, an intermediate azimuth angle image at the same position is required to be imaged; the new image will show two types of grey, this way making it easy to identify the magnetization orientation in this domains.

In XMLD-PEEM, magnetic contrast is achieved from the asymmetry of two images obtained for the same photon polarization at two different energies [95]. A detailed description will be presented in the next chapter.

3.3   A brief description of the setup development

The forthcoming results in this work were sustained by a collaborative work to improve or to build different parts of the chambers. For the synchrotron experiment a UHV chamber equipped with all the facilities of growth and sample characterization was used. The PEEM sample stage had to be adapted that, with no sample inserted, the X rays can pass trough, this way allowing to use the main chamber manipulator to measure the drain current of the sample (for X-ray absorption measurements). Another delicate task was to attach a nitrogen cooling system for the PEEM, necessary for low temperature microscopy experiments. An external VG-cooling system [103] was connected to the PEEM sample stage in a way that the translation and rotation of the sample was still possible. The connection between the cooling reservoir and the sample stage was made *via* a Cu wire with a diameter of 0.7 cm in a way that no stress was induced to the sample piezo-slides.

The experiments not related to synchrotron radiation were carried out on two UHV chambers in MPI-Halle and FUB Berlin. The chamber form Halle was already equipped with all the facilities for growth and sample characterization. It was used for sample preparation, LEED and LEED *I(E)*, and MOKE experiments. We succeeded also building a preparation chamber connected to an existing Omicron STM part. For the work presented in this thesis, it was necessarily to construct a main sample manipulator with translation and rotation of the sample, resistive heating and nitrogen cooling. An *in-situ* MOKE system adapted to the geometry of the chamber and of the manipulator was also constructed. The preparation chamber is separated from the STM part by an automatic valve, allowing to maintain a low pressure in the STM while sample sputtering. For a better handling of the crystal substrate a transfer load-lock was build. This way samples and STM tips can be inserted/taken out in/from the chamber without breaking the vacuum. *In-situ* sample manipulation was supported by two different wobble-sticks [75] and a mechanical hand [103].

For the synchrotron experiments (XAS and PEEM) the chamber was described in the beginning of Chapter 3.